Energy-resolved detection of precipitating electrons of 30–100 keV by a sounding rocket associated with dayside chorus waves

S. Sugo[1], O. Kawashima[1], S. Kasahara[1], K. Asamura[2], R. Nomura[3], Y. Miyoshi[4], Y. Ogawa[5], K. Hosokawa[6], T. Mitani[2], T. Namekawa[1,2], T. Sakanoi[7], M. Fukizawa[7], N. Yagi[7], Y. Fedorenko[8], A. Nikitenko[8], S.Yokota[9], K. Keika[1], T. Hori[4], C. Koehler[10]

[1]The University of Tokyo, Tokyo, Japan, [2]Japan Aerospace Exploration Agency, Kanagawa, Japan, [3]National Astronomical Observatory of Japan, Tokyo, Japan, [4]Nagoya University, Aichi, Japan, [5]National Institute of Polar Research, Tokyo, Japan, [6]The University of Electro-Communications, Tokyo, Japan, [7]Tohoku University, Miyagi, Japan, [8]Polar Geophysical Institute, Russia, [9]Osaka University, Toyonaka, Japan, [10]University of Colorado at Boulder, USA

Key Points:

- The relation between energetic electron precipitation and chorus waves at the dayside magnetosphere have not been identified in detail
- Our sounding rocket experiment identified precipitating energetic electrons within typical resonance energy with chorus waves on the dayside
- Ground-based and satellite observations of chorus waves support that the observed electron precipitation was caused by chorus waves

Abstract

Whistler mode chorus waves scatter magnetospheric electrons and cause precipitation into the Earth's atmosphere. Previous measurements showed that nightside chorus waves are indeed responsible for diffuse/pulsating aurora. Although chorus waves and electron precipitation have also been detected on the dayside, their link has not been illustrated (or demonstrated) in detail compared to the nightside observations. Conventional low-altitude satellite observations do not well resolve the energy range of 10–100 keV, hampering verification on resonance condition with chorus waves. In this paper we report observations of energetic electrons with energies of 30–100 keV that were made by the electron sensor installed on the NASA's sounding rocket RockSat-XN. It was launched from the Andøya Space Center on the dayside (MLT ~ 11 h) at the L-value of ~ 7 on 13 January 2019. Transient electron precipitation was observed at ~ 50 keV with the duration of <100 s. A ground station at Kola peninsula in Russia near the rocket's footprint observed intermittent emissions of whistler-mode waves simultaneously with the rocket observations. The energy of precipitating electrons is consistent with those derived from the quasi-linear theory of pitch angle scattering by chorus waves through cyclotron resonance, assuming a typical dayside magnetospheric electron density. Precise interaction region is discussed based on the obtained energy spectrum below 100 keV.

Plain Language Summary

The Earth's magnetosphere was filled with energetic electrons and various waves. Energetic electrons sometimes precipitate into the Earth's atmosphere and cause aurora. Whistler mode waves are believed to cause such precipitation and previous measurements showed that nightside chorus waves are responsible for aurora. Energetic electrons and chorus waves are also observed on the dayside magnetosphere. However, their link has not been illustrated in detail compared to the nightside observations. In this paper, we verified the energy spectrum of precipitating electrons on the dayside by installing the sensor which can resolve the 30–100 keV energy range on a sounding rocket and observed transient electron precipitation.

1 Introduction

Precipitating electrons from the magnetosphere have been measured by balloons, sounding rockets, and low-altitude satellites to investigate auroral zone phenomenology [e.g., *Winningham et al.*, 1985; *Fuller-Rowell and Evans*, 1987; *Miyoshi et al.*, 2010, 2015a], radiation belt dynamics [e.g. *Millan and Thorne*, 2007; *Miyoshi et al*., 2008] and effects on the chemical composition of the upper atmosphere [e.g., *Thorne et al.*, 1977; *Lam et al.*, 2010; *Miyoshi et al*., 2015b; *Turunen et al*., 2016]. Hardy et al. [2008] conducted statistical studies based on the large database of energy spectra in the 50 eV–20 keV energy range accumulated by the Defense Meteorological Satellite Program (DMSP) and reported the distributions of electron precipitation depend on geomagnetic latitude (MLAT), magnetic local time (MLT) and Kp index.

Millan and Thorne [2007] reviewed observations of higher energy (~10s keV to ~MeV) electron precipitation as one of the radiation belt electron loss mechanisms. Quasi-periodic bursts of high-energy electron precipitation with short timescale (< 1s), called microbursts, were detected in balloon experiments and the SAMPEX satellite observations [e.g. *Anderson and Milton*, 1964; *Parks*, 1978; *Blake et al.*, 1996]. Statistical surveys from NOAA Polar Orbiting Environmental Satellites (POES) presented the global model of the energy-

integrated flux (> 30 keV) of precipitating electrons as a function of geomagnetic activity [*Lam et al.*, 2010].

Whistler mode chorus waves are believed to play an important role in these electron precipitations. Chorus waves are electromagnetic emissions often composed of discrete rising or falling elements [e.g. *Burtis and Helliwell,* 1969; *Sazhin and Hayakawa,* 1992; *Santlic et al.,* 2003]. The typical frequency of chorus waves is 0.1-0.8 f_{ce}, where f_{ce} is the equatorial electron cyclotron frequency, and has a frequency gap at ~0.5 f_{ce} [e.g. *Burtis and Helliwell,* 1969; *Tsurutani and Smith,* 1974; *Sazhin and Hayakawa,* 1992]. Chorus waves are mostly observed on the nightside during disturbed geomagnetic conditions and confined near the magnetic equator [e.g. *Tsurutani and Smith,* 1977; *Meredith et al.*, 2012]. *Meredith et al.* [2012] showed that lower band chorus (0.1–0.5 f_{ce}) is confined to less than 15° in MLAT on the night side and upper band chorus (0.5–0.8 f_{ce}) is within about 6° in MLAT due to strong Landau damping. Chorus waves are responsible for energetic electron precipitation into the atmosphere by pitch angle scattering. On the nightside, recent evidence suggests that chorus waves are the dominant cause of electron pitch-angle scattering and resulting diffuse/pulsating aurora [e.g. *Ni et al.*, 2008, 2011; *Nishimura et al.,* 2010; *Thorne et al.,* 2010; *Miyoshi et al*., 2015a; *Kasahara et al.,* 2018a; 2019; *Ozaki et al.,* 2019; *Hosokawa et al.,* 2020; *Nishimura et al.*, 2020].

Dayside chorus waves are less dependent on the geomagnetic conditions and were observed over wider range of magnetic latitude than nightside chorus waves [*Tsurutani and Smith,* 1977; *Meredith et al.,* 2012]. *Meredith et al.* [2012] showed that lower band chorus waves were observed up to 30° in MLAT on the dayside. These features derive from the distortion of the dayside magnetic field due to solar wind compression. The distortion forms two minima of magnetic field strength (minimum B pockets) at high latitudes of both hemispheres. Chorus waves can be generated at these regions [*Vaivads et al.,* 2007; *Tsurutani et al.,* 2009]. The distortion also forms the region called Dayside Uniform Zone (DUZ), where the gradient of the magnetic field strength along the field (*dB/ds*) is nearly zero within a large range of magnetic latitude. Such a field line exists in the transition region between the dipole-like field near the Earth and the compressed field with minimum B pockets. Dayside chorus waves near the DUZ region were observed at the ground during quiet geomagnetic conditions [*Keika et al.,* 2012].

Despite such differences, dayside chorus waves are also expected to contribute to energetic electron precipitation in probably the same physical mechanisms as on the nightside. Dayside diffuse aurora by low energy electron precipitation were reported [e.g. *Newell et al.,* 2009; *Han et al.,* 2015] and *Nishimura et al.* [2013] indicated that chorus waves are the dominant cause of dayside diffuse aurora. At high latitude (L>6), <100 keV electrons are expected to efficiently resonate with chorus waves at the magnetic equator and off-equatorial minimum-B pockets and precipitate into the atmosphere. While high energy electrons were observed on the dayside [e.g. *Parks et al.,* 1978; *Lam et al.,* 2010], few previous observations have identified <100 keV because of the lack of energy resolution. Previous researches indirectly obtained precipitated flux in the range of 30–100 keV by subtracting the integral flux of >100 keV from that of >30 keV [*Ni et al.,* 2014; *Li* et al., 2013, 2014a, 2014b]. However, different channels have different efficiencies for incoming electrons and different proton contaminations, which are difficult to correct due to a lack of reliable proton measurements [*Yando et al.,* 2011; *Askainen and Mursula,* 2013], making it difficult to obtain reliable electron energy spectra at 30-100 keV.

In this paper, we investigate the energy spectrum of precipitating electrons of 30-100 keV on the dayside in order to discuss resonance condition. The electron sensor was installed on the

NASA's sounding rocket RockSat-XN, which was launched on the dayside (MLT ~ 11 h) at L ~ 7 from the Andøya Space Center. The electron sensor detected precipitating electrons in the sunlit region, where little research has been done on the precipitating electrons of 30-100 keV. Section 2 describes instrumentation and installation on the sounding rocket. Section 3 provides solar wind, geomagnetic condition and magnetospheric configuration. In section 4, we discuss the resonance condition based on chorus wave frequency measured at a ground station near the rocket's footprint.

2 Instrumentation

Main results in this paper were obtained by Medium-energy Electron Detector (MED). MED can measure the electron velocity distribution functions in the energy range of 30–100 keV. MED is comprised of five pinholes and avalanche photodiodes (APD), covering nearly 2-pi steradian field of view. APDs provide higher signal-to-noise ratio than conventional solid-state detectors because of its internal gain and have advantage of high quantum efficiency for a few tens of keV electrons [*Ogasawara et al.*, 2005, 2006, 2008, 2016; *Kasahara et al.*, 2010, 2012]. We utilized APDs with the thickness of ~70 μm to properly measure the incoming energy for 30–100 keV electrons. To attenuate protons and photons, APDs were covered by ~2 μm aluminum layer. Preamplifiers, shaping amplifiers, peak holders, and analog-to-digital converters are used to measure the incoming electron energy. Detected signals are binned into logarithmically separated sixteen pulse height channels depending on the incoming electron energy. A geometric factor of MED was 7.7×10^{-5} cm^2 sr per APD. Energy resolution was about 50% (<10 keV) at half maximum for 20 keV electrons. Because higher energy electron is less dependent on attenuation by aluminum layer, energy resolution is higher for higher energy electron. For example, energy resolution was about 10% for 30 keV and about 2% for 100 keV in Monte Carlo simulation.
MED was installed on the sounding rocket in such a way that the angles between looking direction of five APDs and the rocket spin axis were 30°, 30°, 90°, 150° and 150°. Fluxgate magnetometer was also mounted on the rocket. The RockSat-XN rocket was launched from Andøya Space Center in Norway at 0913 UT on 13 January 2019. The hemispherical field of view of MED covered most of the pitch angle range by the rocket spinning and coning, whose periods are ~1 s and ~30 s, respectively. We determined pitch angles by using the Fluxgate magnetometer, which was also onboard the rocket.

3 Observation

3.1. Solar Wind and Geomagnetic Condition

Figure 1 shows solar wind data from the WIND spacecraft between 0300 and 1600 UT on 13 January 2019. A black dashed line indicates the launch time. Figure 1 (a) shows that Ygsm component of the interplanetary magnetic field was negative and Zgsm component fluctuated within ± 3 nT. Figure 1 (b) and (c) show that the solar wind velocity was 340 km/s and ion density was 5 cm^{-3}, and the dynamic pressure was ~1 nPa.

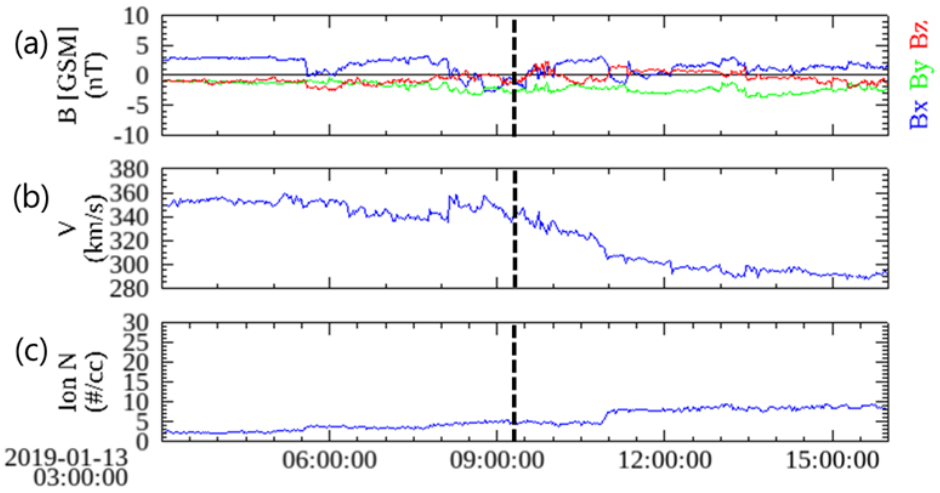

Figure 1. Time profile of the solar wind data from the WIND spacecraft between 0300 and 1600 UT on 13 January 2019. A black dashed line indicates the launch time of the RockSat-XN rocket. (a) Three components of the interplanetary magnetic field in geocentric solar magnetospheric coordinates. (b) Solar wind velocity data of the SWE instrument. (c) Ion density obtained from the MFI, SWE and 3DP instruments.

Figure 2 presents real-time AE index on 13 January 2019. The AE index was steady below 300 nT through the day of flight, but with small increase up to ~200 nT around 0500 UT. The 3-hourly Kp index was in the range of 0 to 1 on 13 January 2019. These data suggest that the period of flight was quiet in terms of solar wind and ground-based geomagnetic conditions.

3.2. Magnetospheric electrons

Figure 3 provides energy-time spectrogram of the spin-averaged electron energy flux from MEP-e [*Kasahara et al.*, 2018a] onboard the ERG satellite [*Miyoshi et al.*, 2018a]. ERG located at (X, Y, Z)gsm = (-1, 6, 1) R_E and at the L-value of 6 around 0900 UT. The perigee and the apogee are (X, Y, Z)gsm = (-1, 0, 0) R_E around 1200 UT and (X, Y, Z)gsm = (5, 2, 2) R_E around 0800 UT respectively. In this figure, it can be seen that ~30-40 keV electron energy flux increased at ~0800 UT and lower energy electron flux also increased later. This suggests that energetic electron injection into the magnetosphere occurred before 0800 UT. This injection may be associated with the small increase of the AE index at ~0500UT.

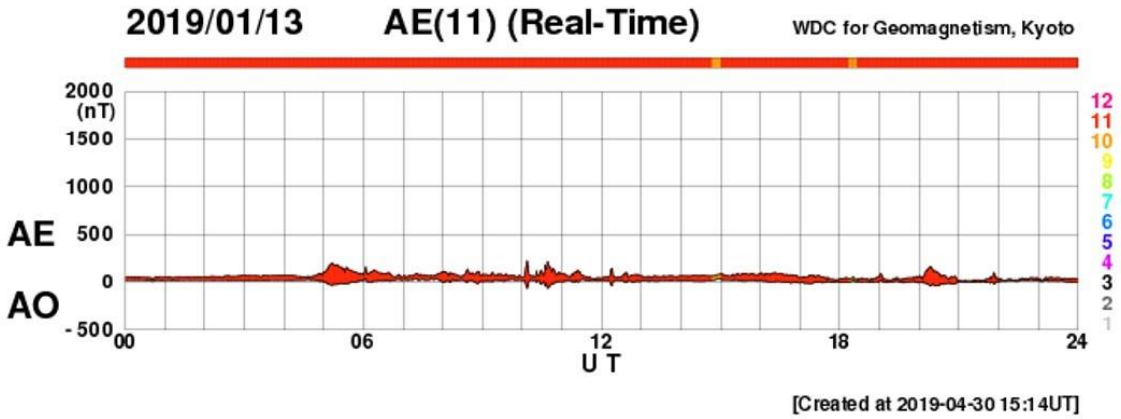

Figure 2. One-day plot of the real-time AE and AO index on 13 January 2019. Color represents the number of stations to derive the index. Color scale is displayed on the right side of panel. There is small substorm event at ~0500 UT.

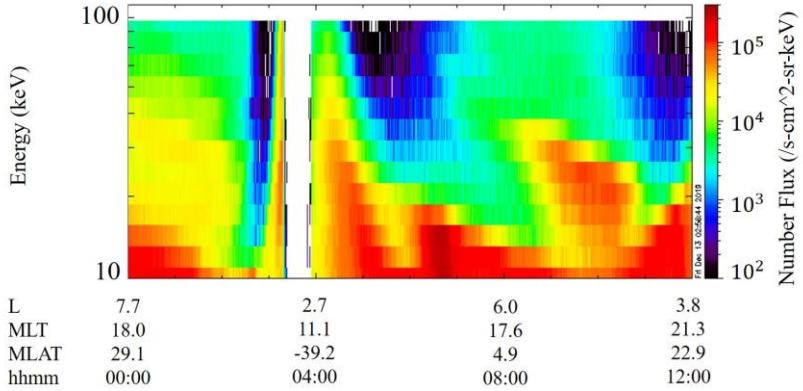

Figure 3. Energy-time spectrogram of the spin-averaged electron energy flux from MEP-e onboard the ERG satellite on 13 January 2019. Enhancement of energetic electron flux was observed between 0800 and 1100 UT. L is the McIlwain L-shell derived from IGRF.

3.3. Rocket observations

NASA's sounding rocket, RockSat-XN was launched at Andøya in Norway (69°17' N, 16°01' E) at 09:13 UT (10:13 LT) on 13 January 2019. Figure 4 shows that the altitude profile of this flight and the horizontal trajectory in the geographical coordinate. Figure 5 (a)–(e) present raw data energy spectra of pitch angles 0–90° (red) and 90–180° (blue) observed by MED for every 50 s from 120 s after the launch, where count rate is divided by the number of channels within 0–85° and 95–180° respectively. Pulse height channels are essentially proportional to the incoming energy. We do not discuss pulse height channels 0–2 because of the high noise level. As shown in Figures 5 (a), (b), (d), and (e), no significant difference between 0–85° and 95–180° spectra during most periods (120–220 s, 270–370 s after launch). This suggests that the detected signals were due to penetrating particles, whose incoming directions were not limited by the pinholes. We estimated count rates and energy deposit caused by penetrating galactic cosmic ray (GCR) proton. Count rates of GCR detected by APDs (size is 0.25 cm^2) is estimated to be ~ 30 counts / 50 s, assuming typical GCR flux ~0.4 / cm^2-s-sr in the solar minimum at the high latitude [*Neher et al.*, 1956], consistent with our observation. Energy deposit is ~30 keV, assuming that GCR with typical energy (~0.1–10 GeV) penetrating the 70 μm silicon APD, consistent with peak

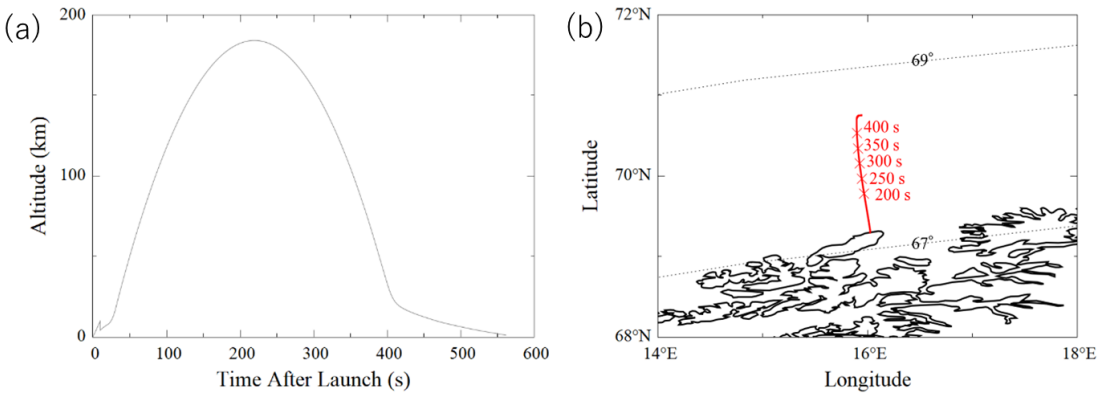

Figure 4. The rocket trajectory. (a) The altitude profile of the RockSat-XN rocket. (b) The position in the geographical coordinate (red line). Five cross marks shows the position 200, 250, 300, 350 and 400 s after launch. Black dotted lines represent geomagnetic latitude.

energy of energy spectra of pitch angle 0–85° and 95–180° (i.e., pulse height channel 7 corresponds to about 30 keV). Therefore, we conclude that most counts during 120–220 s and 270–370 s after the launch are due to GCR. Although upward-looking APDs may have detected precipitating electrons as well, the precipitating electron flux level was too low to be distinguished from GCR for most of the time.

Nevertheless, during 220–270 s after the launch (Figure 5c), counts of pitch angle 0–85° are significantly higher than those of pitch angle 95–180° at pulse height channels 9–12. For this time period, electrons of pitch angles 0–85° show a peak at the different energy from GCR's energy deposit, indicating the transient significant electron precipitation. In order to confirm that two spectra are different, we conducted the Kolmogorov–Smirnov statistical test, which examines null hypothesis that energy spectra of pitch angles 0–85° and 95–180° come from the same population. The null hypothesis was rejected with significance level of ~0.4 %. Furthermore, we assume that the spectrum of GCR was constant during the whole flight period and averaged the energy spectra of pitch angle 0–85° for 120–370 s, so that the error of the energy spectrum of GCR becomes less (Figure 5f, blue line). We performed the Kolmogorov–Smirnov test again for the averaged spectrum of GCR and that of pitch angle 0–85° during 220–370 s after launch as well and rejected the null hypothesis with significance level of ~0.4%. No significant difference was found between spectra of pitch angle 0–85° and GCR during the other periods. These data indicate that there was a transient electron precipitation within ~100 s.

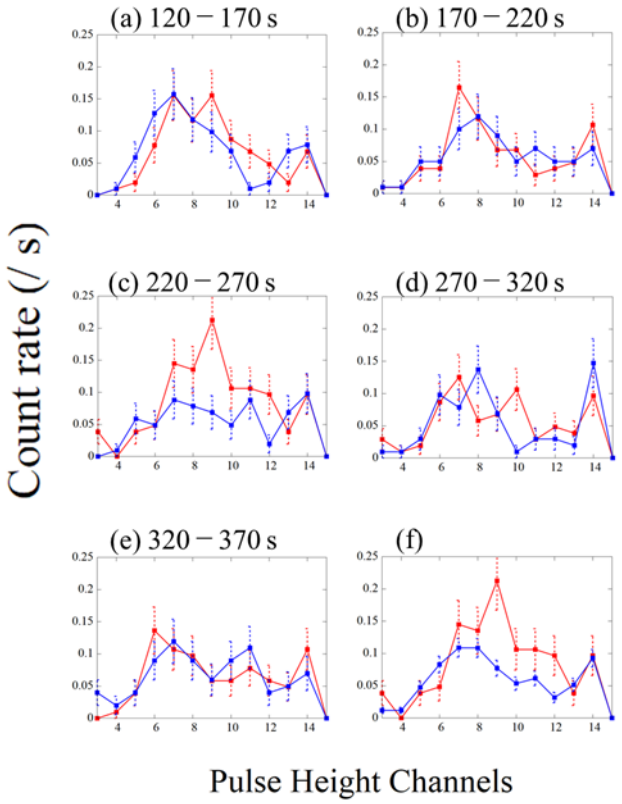

Figure 5. Energy spectra of pitch angles 0–85° (red) and 95-180° (blue) observed by MED during (a) 120–170 s, (b) 170–220 s, (c) 220–170 s, (d) 270–320 s, (e) 320–370 s, after the launch. Standard deviation assuming Poisson distribution counting statistics are shown by error bars. Pulse Height Channels are essentially proportional to the detected energy. The count rate is calculated by dividing the count detected by the five detectors facing the pitch angles of 0-85° or 95-180° by the observation time. (f) Energy spectrum of pitch angle 0–85° during 220–270 s (red) and that of pitch angle 95–180° for 120-370 s (blue).

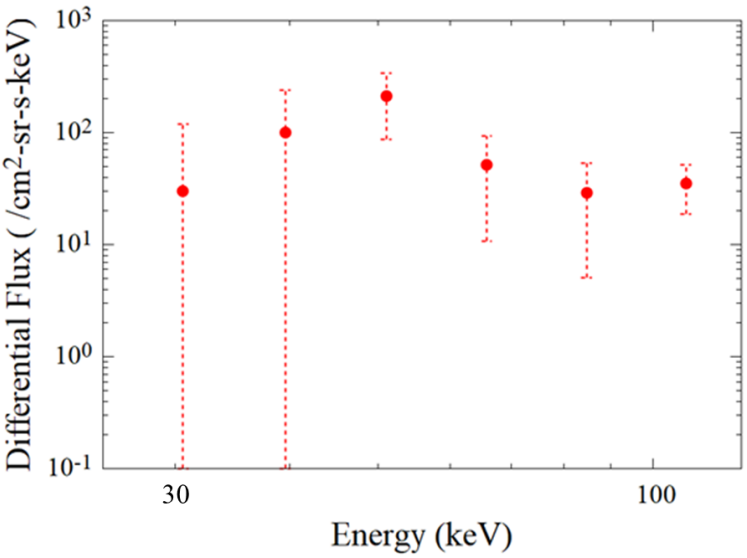

Figure 6. Calibrated energy spectrum of precipitating electrons. Error bars indicate 2σ, where σ is the standard error.

We calibrated pulse height channel to energy and counts to differential flux based on the geometrical design and laboratory tests. Note that here we obtain the precipitating electron counts by subtracting GCR contamination (Figure 5f, blue line) from the counts in the pitch angle 0–85° during 220–270 s (Figure 5f, red line). Thus, obtained energy spectrum is shown in Figure 6, illustrating that the differential flux of precipitating electron is ~10^2 /cm^2-sr-s-keV at 50 keV. The differential electron flux is comparable to that derived from an electron density profile measured with the Tromsø EISCAT VHF radar at the same time, assuming that an increase of electron density is mainly due to electron precipitation.

4 Discussion

We investigated the precipitating electrons on the dayside by using the energetic electron detector which can observe energy spectrum of 30–100 keV electrons, and found precipitating electrons peaking at ~50 keV. Here we discuss whether this electron precipitation can be explained by the pitch angle scattering by chorus waves.
Figure 7 provides a frequency-time spectrogram, showing the magnetic field emissions obtained by the VLF receiver at Lovozero, Kola peninsula in Russia (*L*~5.4, LT~11 h) near the rocket trajectory around the time of electron precipitation. The difference in longitude was less than 15°. Although this receiver observation is not strictly conjugated with the RockSat-XN measurements, it is helpful to infer whistler-mode wave occurrence in the flux tube on which RockSat-XN was located. The footprint of Lovozero was traced to the magnetic equator along field line using the Tsyganenko T89 model [*Tsyganenko* 1988] to evaluate the condition of cyclotron resonance between electrons and VLF emissions. The obtained magnetic field strength is ~220 nT near the magnetic equator, corresponding to the cyclotron frequency f_{ce} of 6.2 kHz. Waves were seen at ~0.2 – 0.8 f_{ce} with a band gap at ~ 0.5 f_{ce}, typical of chorus waves.

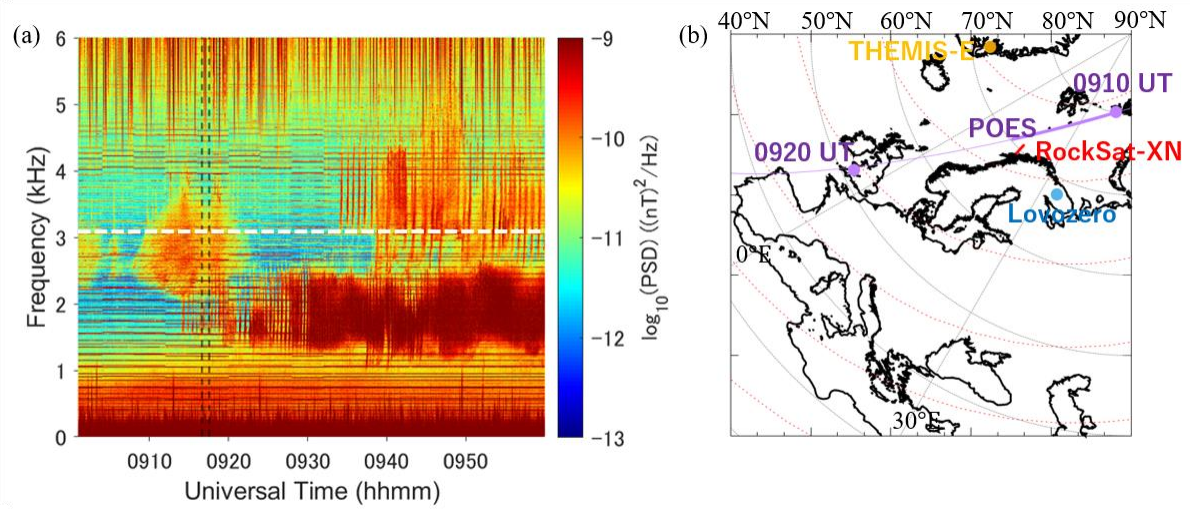

Figure 7. (a) Power spectrogram of magnetic field obtained by the VLF receiver at Lovozero in Russia between 0900 and 1000 UT on 13 January 2019. Vertical dotted lines show 220 s and 270s after the launch of RockSat-XN. The horizontal dotted line shows 3.1 kHz, which is 0.5 f_{ce} near the magnetic equator of the field line extending from Lovozero. (b) The rocket trajectory and positions of the VLF receiver at Lovozero, THEMIS-E footprint and POES footprint in geographical coordinate (black dotted lines). Red dotted lines show geomagnetic latitude (25°, 35°, 45°, 55°, 65°, 75°). Two purple points shows POES footprints at 0910 and 0920 UT. The thick purple line shows POES NOAA-18 footprint between 0910 and 0914 UT, when electron precipitation events were seen from the data of the Medium Energy Proton and Electron Detector (MEPED) on board the POES satellite.

Chorus waves were also observed in the magnetosphere. Figure 8 shows the energy-time spectrogram of electrons and frequency-time spectrograms of the wave electric field and wave magnetic field, observed by THEMIS-E satellite [*Angelopoulos*, 2008]. THEMIS-E was located near the dawnside magnetopause as can be seen from the intermittent excursions to the magnetosheath in Figures 8a and b. Figures 8c and d show electromagnetic waves at $0.1 - 0.6\ f_{ce}$ in the magnetosphere, where f_{ce} is ~360 Hz at the minimum magnetic field strength along the magnetic flux tube on which THEMIS-E was located, especially at 0918, 0937 and 0954 UT. To combine, ground-based and magnetospheric observations suggest that VLF emissions were generated broadly in the dayside magnetosphere during this period.

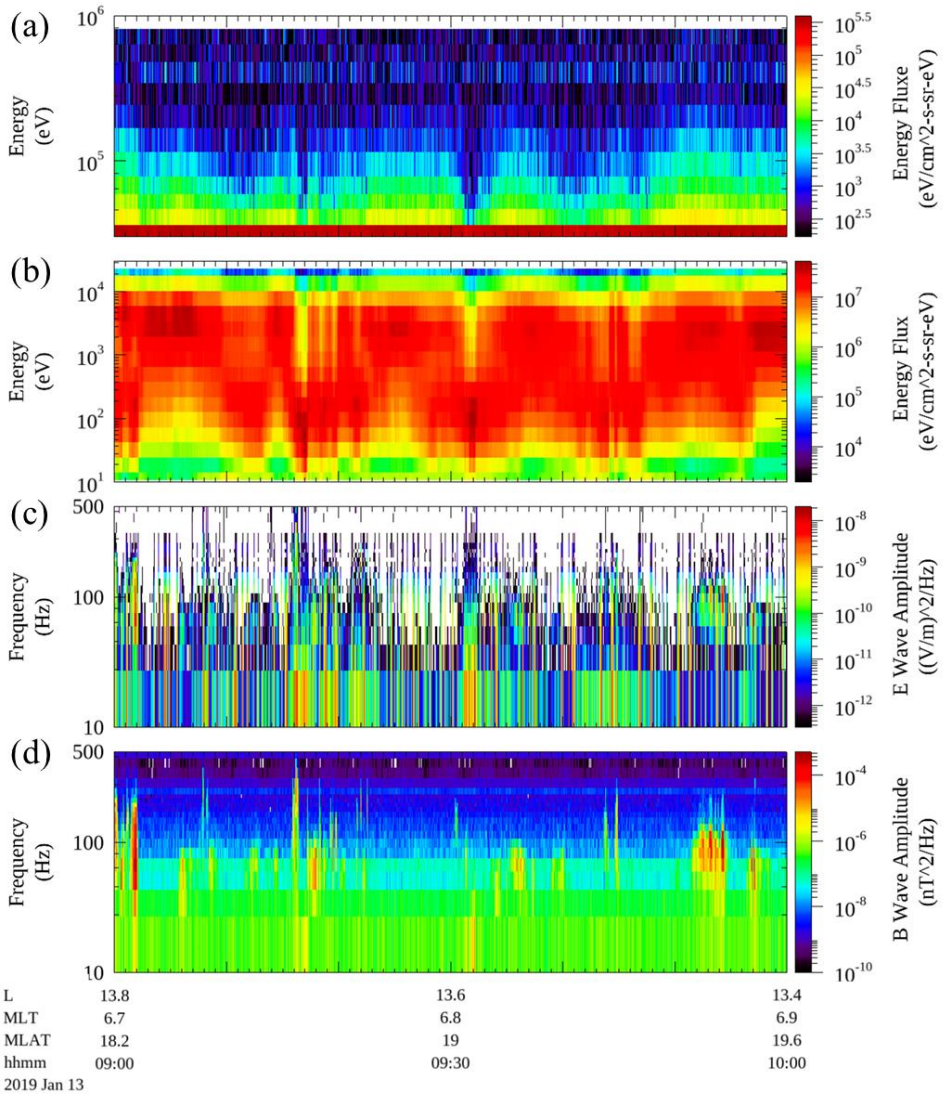

Figure 8. Electron energy-time spectrograms of (a) high energy (from the SST instrument) and (b) low energy (the ESA instrument) components, and frequency-time spectrograms of (c) electric field (from EFI) and (d) magnetic field (SCM), obtained by the THEMIS-E spacecraft during 0900 to 1000 UT on 13 January 2019. THEMIS-E located at (X, Y, Z)sm = (4, -12, 3)R_E around 0900 UT.

Assuming that observed precipitating ~ 50 keV electrons was scattered at magnetic equator by lower band chorus waves with $0.1 - 0.5\ f_{ce}$, we can estimate a plasma density by using general resonance condition and the standard cold plasma dispersion relation [e.g. *Summers et al.*, 1998]. We use the magnetic field strength ~100 nT at the magnetic equator of the rocket's footprint. The calculated plasma density was 4 cm^{-3} and 0.4 cm^{-3} assuming chorus waves with ~0.1 f_{ce} and 0.5 f_{ce}, respectively. To compare, the density observed by the THEMIS-E ESA, which was located at higher L than the rocket trajectory, was 1 - 2 cm^{-3}. In addition, the typical plasma density is 5.6±1.7 cm^{-3} at L~6.9 and LT~10 h according to the statistical study by *Sheeley et al.* [2001]. The above calculated plasma density 4 cm^{-3} is consistent with these values, thus 0.1 f_{ce} chorus waves is favored for equatorial scattering.

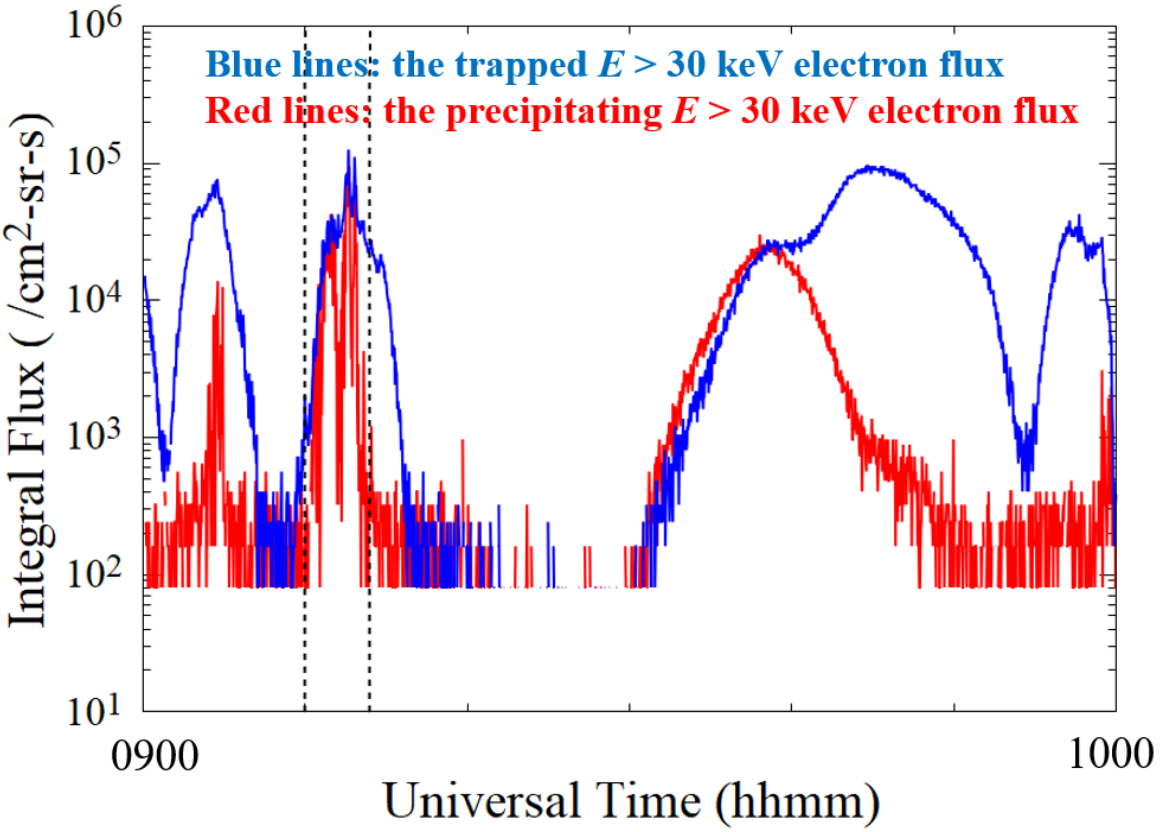

Figure 9. The trapped E > 30 keV electron flux (blue lines) and the precipitating E > 30 keV electron flux (red lines) measured by MEPED onboard the POES NOAA-18 during 0900 to 1000 UT on 13 January 2019. Vertical dotted lines show 0910 and 0914 UT.

The above scenario, the equatorial resonance with 0.1 f_{ce} chorus waves, reasonably explains the precipitation of electrons of ~50 keV. However, it may contradict with the observed energy spectrum peaking at ~ 50 keV. Considering that the flux of 30 keV is typically higher than that of 50 keV in the quiet magnetosphere, and lower band chorus waves with >0.2 f_{ce} can interact with ~30 keV electrons near the magnetic equator for the same condition, the precipitation flux peak at ~ 50 keV is not expected. While the apparent peak at ~ 50 keV is due to the insufficient statistics (the flux difference was within 2σ between 30 and 50 keV), here we briefly discuss other possible explanations. One possibility is that the density significantly deviates from the typical value. When the density is 0.1 cm^{-3}, lower band chorus waves with 0.1 - 0.5 f_{ce} can resonate with 50 - 700 keV electrons and not with <50 keV electrons. However, such a low density is inconsistent with the observation by THEMIS-E and hence we think it is unlikely. Another possible case is that resonance occurred only at the high magnetic latitude, where the magnetic field is stronger than the magnetic equator. Suppose the chorus waves of < 0.5 f_{ce} were generated at the equator in the slightly higher L-shell region (e.g., the magnetic field intensity ~ 70 nT) and obliquely propagated to the magnetic field line of the rocket trajectory, up to the latitude of 25° (the magnetic field intensity ~ 180 nT), the 30 keV electrons becomes out of resonance any more [e.g., *Miyoshi et al.*, 2015b]. In fact, significant wave power of chorus waves with less frequency than a typical band gap ~0.5 f_{ce} are frequently observed at magnetic latitudes >15° on the dayside [*Meredith et al*., 2014]. Therefore, the off-equatorial scattering by obliquely propagating chorus waves may be a more plausible scenario than the equatorial scattering, at least for this case, in contrast to the statistical view on the nightside [*Kasahara et al*., 2019].

Figure 9 shows the trapped and precipitating electron fluxes (>30 keV) measured by MEPED onboard the POES NOAA-18 [*Evans and Greer,* 2000]. The precipitating electron flux was high during 0910 to 0914 UT, when the trajectory of the POES satellite is shown in the thick purple line of Figure 7b. This indicates that the precipitation extended to higher L-shell region, consistent with the chorus emission observed by THEMIS-E. The precipitation was intermittent, which is also consistent with our observation.

Figure 9 shows that the >30 keV integrated flux of precipitating electrons was ~$10^{4\text{-}5}$ /cm^2-sr-s. Furthermore, statistical surveys on the >30 keV electron precipitation showed that the integrated flux of precipitating electrons is typically ~10^4 /cm^2-sr-s at $L > 6$ on the dayside under quiet geomagnetic condition (AE<100 nT) [*Lam et al.,* 2010]. The precipitation event observed by MED showed that integrated flux of precipitating electron was ~10^4 /cm^2-sr-s in 30–100 keV, which is lower than observed by POES. This indicates that electron precipitation was intense at higher latitude where POES was located during 0910 to 0914 UT supporting the scenario that chorus waves obliquely propagate to inside and scatter the electrons at the magnetic field line of the rocket trajectory.

The duration of the precipitating event was <100 s at RockSat-XN. One of possible causes of this short period precipitation is the temporal variation of chorus waves. Chorus waves propagated to Lovozero which have quasi-periodic variations with a timescale ~50 s as can be seen in Figure 7. The intermittent variations of chorus waves may have corresponded to the transient electron precipitation. Nevertheless, quasi-periodicity ~50 s was not found in electron precipitation at RockSat-XN. We infer that chorus waves may have ceased temporarily and locally at the rocket's magnetospheric footprint.

5 Conclusions

There have been several observations of chorus waves and precipitating electrons on the dayside, while their relation has not been verified quantitatively due to the insufficient energy resolution of conventional low-altitude satellites in the range of 10s-100s keV. Using the medium-energy electron detector sensitive to 30–100 keV onboard the sounding rocket RockSat-XN, we confirmed the electron precipitation in the range of typical resonance energy with chorus waves on the dayside during the geomagnetically quiet periods. Chorus waves were observed by the ground-based VLF receiver in Lovozero near the launch site and THEMIS-E spacecraft in the dayside magnetosphere around the period of the precipitation event. The electron energy is consistent with the resonance energy derived from quasi-linear theory of magnetospheric electron scattering by chorus waves through cyclotron resonance. The detailed energy spectrum below 100 keV enabled the discussion suggesting the possible location of wave-particle interaction.

Acknowledgments, Samples, and Data

We are grateful for the support of NASA Wallops Flight Facility's (WFF) and Andøya Space Center (ASC). This study was supported by JSPS Bilateral Open Partnership Joint Research Projects. This study is supported by JSPS Kakenhi (15H05747, 16H06286, 20H01959 and 26707026). The rocket and instruments' data used in this study are available at the UTokyo Repository (http://hdl.handle.net/2261/00079366). The data of VLF receiver used in this paper are available at the site (http://aurora.pgia.ru/erg-pgi/case1.html). Wind data are available through Coordinated Data Analysis Web (CDAWeb), NASA. The AE index used in this paper was provided by the WDC for Geomagnetism, Kyoto (http://wdc.kugi.kyoto-u.ac.jp/wdc/Sec3.html). Science data of the ERG (Arase) satellite were obtained from the ERG Science Center operated by ISAS/JAXA and ISEE/Nagoya University (https://ergsc.isee.nagoya-u.ac.jp/index.shtml.en; *Miyoshi et al*, 2018b). The present study

analyzed the MEP-e L2-v01_01 data and orb L2 data obtained by ERG. The present study used SPEDAS for the data analysis [*Angelopoulos et al*., 2019]. We acknowledge NASA contract NAS5-02099 for use of data from the THEMIS mission; specifically, J. W. Bonnell and F. S. Mozer for use of EFI data, C. W. Carlson and J. P. McFadden for use of ESA data, A. Roux and O. LeContel for use of SCM data provided under the lead of the Technical University of Braunschweig and with financial support through the German Ministry for Economy and Technology and the German Center for Aviation and Space (DLR) under contract 50 OC 0302. The authors thank the NOAA National Centers for Environmental Information (NCEI) for providing NOAA POES and documentation (https://cdaweb.gsfc.nasa.gov/istp_public/data//noaa/noaa18/sem2_fluxes-2sec/2019/noaa18_poes-sem2_fluxes-2sec_20190113_v01.cdf).

References

Anderson, K. A., & Milton, D. W. (1964). Balloon Observations of X Rays in the Auroral Zone 3. *Journal of Geophysical Research: Space Physics*, *69*(21). https://doi.org/10.1029/JZ069i021p04457

Angelopoulos, V. (2008). The THEMIS mission. Space Science Reviews (Vol. 141). https://doi.org/10.1007/s11214-008-9336-1

Angelopoulos, V., Cruce, P., Drozdov, A., Grimes, E. W., Hatzigeorgiu, N., King, D. A., et al. (2019). The Space Physics Environment Data Analysis System (SPEDAS). Space Science Reviews (Vol. 215). The Author(s). https://doi.org/10.1007/s11214-018-0576-4

Asikainen, T., & Mursula, K. (2011). Recalibration of the long-term NOAA/MEPED energetic proton measurements. *Journal of Atmospheric and Solar-Terrestrial Physics*, *73*(2–3), 335–347. https://doi.org/10.1016/j.jastp.2009.12.011

Asikainen, T., & Mursula, K. (2013). Correcting the NOAA/MEPED energetic electron fluxes for detector efficiency and proton contamination. *Journal of Geophysical Research: Space Physics*, *118*(10), 6500–6510. https://doi.org/10.1002/jgra.50584

Blake, J. B., Looper, M. D., Baker, D. N., Nakamura, R., Klecker, B., & Hovestadt, D. (1996). New high temporal and spatial resolution measurements by SAMPEX of the precipitation of relativistic electrons. *Advances in Space Research*, *18*(8), 171–186. https://doi.org/10.1016/0273-1177(95)00969-8

Burtis, W. J., & Helliwell, R. A. (1969). Banded Chorus. a New Type of Vlf Radiation Observed in the Magnetosphere By Ogo 1 and Ogo 3.*Journal of Geophysical Research:*, *74*(11), 3002–3010. https://doi.org/10.1029/ja074i011p03002

Evans, D. S., & Greer, M. S. (2000). Polar Orbiting Environmental Satellite Space Environment Monitor - 2 : Instrument Descriptions and Archive Data Documentation, Tech. Memo. OAR SEC-93, NOAA, Boulder, Colo.

Evans, D. S., & Moore, T. E. (1979). Precipitating Electrons Associated With the Diffuse Aurora: Evidence for Electrons of Atmospheric Origin in the Plasma Sheet. *Journal of Geophysical Research*, *84*(A11), 6451–6457. https://doi.org/10.1029/JA084iA11p06451

Fuller-Rowell, T. J., & Evans, D. S. (1987). Height-integrated Pedersen and Hall conductivity patterns inferred from the TIROS-NOAA satellite data. *Journal of Geophysical Research*, *92*(A7), 7606. https://doi.org/10.1029/ja092ia07p07606

Han, D., X.-C. Chen, J.-J. Liu, Q. Qiu, K. Keika, Z.-J. Hu, J.-M. Liu, H.-Q. Hu, and H.-G. Yang (2015), An extensive survey of dayside diffuse aurora based on optical observations at Yellow River Station, *Journal of Geophysical Research:Space Physics*, *120*, 7447‐7465, https://doi.org/10.1002/2015JA021699

Hardy, A., Holeman, E. G., Burke, W. J., Gentile, L. C., & Bounar, K. H. (2008). Probability distributions of electron precipitation at high magnetic latitudes. *Journal of Geophysical Research: Space Physics*, *113*(6), 1–19. https://doi.org/10.1029/2007JA012746

Hosokawa, K., Miyoshi, Y., Ozaki, M., Oyama, S. I., Ogawa, Y., Kurita, S., et al. (2020). Multiple time-scale beats in aurora: precise orchestration via magnetospheric chorus waves. *Scientific Reports*, *10*(1), 3380. https://doi.org/10.1038/s41598-020-59642-8

Kasahara, S., Takashima, T., & Hirahara, M. (2012). Variability of the minimum detectable energy of an APD as an electron detector. *Nuclear Instruments and Methods in Physics Research, Section A: Accelerators, Spectrometers, Detectors and Associated Equipment*, *664*(1), 282–288. https://doi.org/10.1016/j.nima.2011.11.033

Kasahara, S., Yokota, S., Mitani, T., Asamura, K., Hirahara,M., Shibano, Y., & Takashima, T. (2018). Medium-energy particle experiments—electron analyzer (MEP-e) for the exploration of energization and radiation in geospace (ERG) mission. *Earth, Planets and Space*, *70*(1), 1–16. https://doi.org/10.1186/s40623 - 018 - 0847 - z

Kasahara, S., Miyoshi, Y., Yokota, S., Mitani, T., Kasahara, Y., Matsuda, S., et al. (2018). Pulsating aurora from electron scattering by chorus waves. *Nature*, *554*(7692), 337–340. https://doi.org/10.1038/nature25505

Kasahara, S., Miyoshi, Y., Kurita, S., Yokota, S., Keika, K., Hori, T., et al (2019). Strong diffusion of energetic electrons by equatorial chorus waves in the midnight - to - dawn sector. *Geophysical Research Letters*, *46*. https://doi.org/10.1029/2019GL085499

Kasahara, S, Takashima, T., Asamura, K., & Mitani, T. (2010). Development of an APD with large area and thick depletion layer for energetic electron measurements in space. *IEEE Transactions on Nuclear Science*, *57*(3 PART 3), 1549–1555. https://doi.org/10.1109/TNS.2010.2047752

Keika, K., Spasojevic, M., Li, W., Bortnik, J., Miyoshi, Y., & Angelopoulos, V. (2012). PENGU In/AGO and THEMIS conjugate observations of whistler mode chorus waves in the dayside uniform zone under steady solar wind and quiet geomagnetic conditions. *Journal of Geophysical Research: Space Physics*, *117*(7), 1–15. https://doi.org/10.1029/2012JA017708

Lam, M. M., Horne, R. B., Meredith, N. P., Glauert, S. A., Moffat-Griffin, T., & Green, J. C. (2010). Origin of energetic electron precipitation >30 keV into the atmosphere. *Journal of Geophysical Research A: Space Physics*, *115*(A4), 1–15. https://doi.org/10.1029/2009JA014619

Lampton, M. (1967). Daytime observations of energetic auroral-zone electrons. *Journal of Geophysical Research*, *72*(23), 5817–5823. https://doi.org/10.1029/jz072i023p05817

Li, W., Thorne, R. M., Bortnik, J., Reeves, G. D., Kletzing, C. A., Kurth, W. S., et al. (2013). An unusual enhancement of low-frequency plasmaspheric hiss in the outer plasmasphere associated with substorm-injected electrons. *Geophysical Research Letters*, *40*(15), 3798–3803. https://doi.org/10.1002/grl.50787

Li, W., Ni, B., Thorne, R. M., Bortnik, J., Green, J. C., Kletzing, C. A., et al. (2013). Constructing the global distribution of chorus wave intensity using measurements of electrons by the POES satellites and waves by the Van Allen Probes. *Geophysical Research Letters*, *40*(17), 4526–4532. https://doi.org/10.1002/grl.50920

Li, W., B. Ni, R. M. Thorne, J. Bortnik, Y. Nishimura, J. C. Green, C. A. Kletzing, W. S. Kurth, G. B. Hospodarsky, H. E. Spence, G. D. Reeves, J. B. Blake, J. F. Fennell, S. G. Claudepierre, and X. Gu (2014), Quantifying hiss-driven energetic electron precipitation: A detailed conjunction event analysis, *Geophys. Res. Lett.*, *41*, 1085‑1092, https://doi.org/10.1002/2013GL059132

Meredith, N. P., Horne, R. B., Sicard-Piet, A., Boscher, D., Yearby, K. H., Li, W., & Thorne, R. M. (2012). Global model of lower band and upper band chorus from multiple satellite

observations. *Journal of Geophysical Research: Space Physics*, *117*(10), 1–14. https://doi.org/10.1029/2012JA017978

Meredith, N. P., R. B. Horne, W. Li, R. M. Thorne, and A. Sicard-Piet (2014). Global model of low-frequency chorus (f_{LHR} <f <0.1 f_{ce}) from multiple satellite observations, *Geophysical Research Letters*, *41*, 280‑286, http://doi:10.1002/2013GL059050.

Meredith, N. P., Horne, R. B., Isles, J. D., & Green, J. C. (2016). Extreme energetic electron fluxes in low Earth orbit: Analysis of POES e > 30, e > 100, and e > 300 keV electrons. *Space Weather*, *14*(2), 136–150. https://doi.org/10.1002/2015SW001348

Millan, R. M., & Thorne, R. M. (2007). Review of radiation belt relativistic electron losses. *Journal of Atmospheric and Solar-Terrestrial Physics*, *69*(3), 362–377. https://doi.org/10.1016/j.jastp.2006.06.019

Miyoshi, Y., Sakaguchi, K., Shiokawa, K., Evans, D., Albert, J., Connors, M., & Jordanova, V. (2008). Precipitation of radiation belt electrons by EMIC waves, observed from ground and space. *Geophysical Research Letters*, *35*(23), 1–5. https://doi.org/10.1029/2008GL035727

Miyoshi, Y., Katoh, Y., Nishiyama, T., Sakanoi, T., Asamura, K., & Hirahara, M. (2010). Time of flight analysis of pulsating aurora electrons, considering wave-particle interactions with propagating whistler mode waves. *Journal of Geophysical Research: Space Physics*, *115*(10), 1–7. https://doi.org/10.1029/2009JA015127

Miyoshi, Y., Oyama, S., Saito, S., Kurita, S., Fujiwara, H., Kataoka, R., et al. (2015). Energetic electron precipitation associated with pulsating aurora: EISCAT and Van Allen Probe observations. *Journal of Geophysical Research: Space Physics, 120*(4), 2754–2766. https://doi.org/10.1002/2014JA020690

Miyoshi, Y., Saito, S., Seki, K., Nishiyama, T., Kataoka, R., Asamura, K., et al. (2015). Relation between fine structure of energy spectra for pulsating aurora electrons and frequency spectra of whistler mode chorus waves. *Journal of Geophysical Research: Space Physics*, *120*(9), 7728–7736. https://doi.org/10.1002/2015JA021562

Miyoshi, Y., Shinohara, I., Takashima, T., Asamura, K., Higashio, N., Mitani, T., et al. (2018). Geospace exploration project ERG. *Earth, Planets and Space*, *70*(1). https://doi.org/10.1186/s40623-018-0862-0

Miyoshi, Y., Hori, T., Shoji, M., Teramoto, M., Chang, T. F., Segawa, T., et al. (2018). The ERG Science Center. *Earth, Planets and Space, 70*(1). https://doi.org/10.1186/s40623-018-0867-8

Newell, P. T., Sotirelis, T., & Wing, S. (2009). Diffuse, monoenergetic, and broadband aurora: The global precipitation budget. *Journal of Geophysical Research: Space Physics*, *114*(9), 1–20. https://doi.org/10.1029/2009JA014326

Ni, B., Thorne, R. M., Shprits, Y. Y., & Bortnik, J. (2008). Resonant scattering of plasma sheet electrons by whistler-mode chorus: Contribution to diffuse auroral precipitation. *Geophysical Research Letters*, *35*(11), 1–5. https://doi.org/10.1029/2008GL034032

Ni, B., Thorne, R. M., Meredith, N. P., Horne, R. B., & Shprits, Y. Y. (2011). Resonant scattering of plasma sheet electrons leading to diffuse auroral precipitation: 2. Evaluation for whistler mode chorus waves. *Journal of Geophysical Research: Space Physics*, *116*(4), 1–17. https://doi.org/10.1029/2010JA016233

Ni, B., W. Li, R. M. Thorne, J. Bortnik, J. C. Green, C. A. Kletzing, W. S. Kurth, G. B. Hospodarsky, and M. de Soria-Santacruz Pich (2014), A novel technique to construct the global distribution of whistler mode chorus wave intensity using low-altitude POES electron data, *J. Geophys. Res. Space Physics*, *119*, 5685–5699. https://doi:10.1002/2014JA019935

Nishimura, Y., Bortnik, J., Li, W., Thorne, R. M., Lyons, L. R., Angelopoulos, V., et al. (2010). Identifying the driver of pulsating aurora. *Science*, *330*(6000), 81–84. https://doi.org/10.1126/science.1193186

Nishimura, Y., Bortnik, J., Li, W., Thorne, R. M., Ni, B., Lyons, L. R., et al. (2013). Structures of dayside whistler-mode waves deduced from conjugate diffuse aurora. *Journal of Geophysical Research: Space Physics*, *118*(2), 664–673. https://doi.org/10.1029/2012JA018242

Nishimura, Y., Lessard, M. R., Katoh, Y., Miyoshi, Y., Grono, E., Partamies, N., et al. (2020). Diffuse and Pulsating Aurora. *Space Science Reviews*, *216*(1), 1–38. https://doi.org/10.1007/s11214-019-0629-3

Ogasawara, K., Asamura, K., Mukai, T., & Saito, Y. (2005). Avalanche photodiode for measurement of low-energy electrons. *Nuclear Instruments and Methods in Physics Research, Section A: Accelerators, Spectrometers, Detectors and Associated Equipment*, *545*(3), 744–752. https://doi.org/10.1016/j.nima.2005.02.026

Ogasawara, K., Hirahara, M., Miyake, W., Kasahara, S., Takashima, T., Asamura, K., et al. (2008). High-resolution detection of 100 keV electrons using avalanche photodiodes. *Nuclear Instruments and Methods in Physics Research, Section A: Accelerators, Spectrometers, Detectors and Associated Equipment*, *594*(1), 50–55. https://doi.org/10.1016/j.nima.2008.05.056

Ogasawara, K, Livi, S. A., Allegrini, F., Broiles, T. W., Dayeh, M. A., Desai, M. I., et al. (2016). Journal of Geophysical Research : Space Physics Next-generation solid-state detectors for charged Special Section : *Journal of Geophysical Research: Space Physics*, 1–17. https://doi.org/10.1002/2016JA022559.Abstract

Ogasawara, K., Asamura, K., Takashima, T., Saito, Y., & Mukai, T. (2006). Rocket observation of energetic electrons in the low-altitude auroral ionosphere during the DELTA campaign. *Earth, Planets and Space*, *58*(9), 1155–1163. https://doi.org/10.1186/BF03352005

Ozaki, M., Miyoshi, Y., Shiokawa, K., Hosokawa, K., Oyama, S. ichiro, Kataoka, R., et al. (2019). Visualization of rapid electron precipitation via chorus element wave–particle interactions. *Nature Communications*, *10*(1). https://doi.org/10.1038/s41467-018-07996-z

Parks, G. K. (2013). Microburst Precipitating Phenomena. *Journal of Chemical Information and Modeling*, *53*(9), 1689–1699. https://doi.org/10.1017/CBO9781107415324.004

Santolík, O., Gurnett, D. A., Pickett, J. S., Parrot, M., & Cornilleau-Wehrlin, N. (2003). Spatio-temporal structure of storm-time chorus. *Journal of Geophysical Research: Space Physics*, *108*(A7), 1–14. https://doi.org/10.1029/2002JA009791

Sazhin, S. S., & Hayakawa, M. (1992). Magnetospheric chorus emissions: A review. *Planetary and Space Science*, *40*(5), 681–697. https://doi.org/10.1016/0032-0633(92)90009-D

Sheeley, B. W., Moldwin, M. B., Rassoul, H. K., & Anderson, R. R. (2001). An empirical plasmasphere and trough density model: CRRES pobservations. *Journal of Geophysical Research: Space Physics*, *106*(2000). https://doi.org/10.1029/2000JA000286

Summers, D., Thorne, R. M., & Xiao, F. (1998). Relativistic theory of wave-particle resonant diffusion with application to electron acceleration in the magnetosphere. *Journal of Geophysical Research: Space Physics*, *103*(A9), 20487–20500. https://doi.org/10.1029/98JA01740

Thorne, R. M., Ni, B., Tao, X., Horne, R. B., & Meredith, N. P. (2010). Scattering by chorus waves as the dominant cause of diffuse auroral precipitation. *Nature*, *467*(7318), 943–946. https://doi.org/10.1038/nature09467

Thorne, R. M. (1977). Energetic radiation belt electron precipitation: A natural depletion mechanism for stratospheric ozone. *Science*, *195*(4275), 287–289. https://doi.org/10.1126/science.195.4275.287

Tsurutani, B. T., & Smith, E. J. (1974). Postmidnight chorus: A substorm phenomenon. *Journal of Geophysical Research*, *79*(1), 118–127. https://doi.org/10.1029/ja079i001p00118

Tsurutani, B. T., & Smith, E. J. (1977). Two types of magnetospheric ELF chorus and their substorm dependences. *Journal of Geophysical Research*, *82*(32), 5112–5128. https://doi.org/10.1029/ja082i032p05112

Tsurutani, B. T., Verkhoglyadova, O. P., Lakhina, G. S., & Yagitani, S. (2009). Properties of dayside outer zone chorus during HILDCAA events: Loss of energetic electrons. *Journal of Geophysical Research: Space Physics*, *114*(3), 1–19. https://doi.org/10.1029/2008JA013353

Tsyganenko, N. A. (1989). A magnetospheric magnetic field model with a warped tail current sheet. *Planetary and Space Science*, *37*(1), 5–20. https://doi.org/10.1016/0032-0633(89)90066-4

Turunen, E., Kero, A., Verronen, P. T., Miyoshi, Y., Oyama, S. I., & Saito, S. (2016). Mesospheric ozone destruction by high-energy electron precipitation associated with pulsating aurora. *Journal of Geophysical Research*, *121*(19), 11852–11861. https://doi.org/10.1002/2016JD025015

Vaivads, A., Santolík, O., Stenberg, G., André, M., Owen, C. J., Canu, P., & Dunlop, M. (2007). Source of whistler emissions at the dayside magnetopause. *Geophysical Research Letters*, *34*(9), 1–5. https://doi.org/10.1029/2006GL029195

World Data Center for Geomagnetism, Kyoto, M. Nose, T. Iyemori, M. Sugiura, T. Kamei (2015). Geomagnetic AE index. https://doi:10.17593/15031-54800

Whittaker, I. C., Rodger, C. J., Clilverd, M. A., & Sauvaud, J.-A. (2014). The effects and correction of the geometric factor for the POES/MEPED electron flux instrument using a multisatellite comparison. *Journal of Geophysical Research: Space Physics*, *119*(8), 6386–6404. https://doi.org/10.1002/2014ja020021

Yando, K., Millan, R. M., Green, J. C., & Evans, D. S. (2011). A Monte Carlo simulation of the NOAA POES Medium Energy Proton and Electron Detector instrument. *Journal of Geophysical Research: Space Physics*, *116*(10), 1–13. https://doi.org/10.1029/2011JA016671

Figure 1.

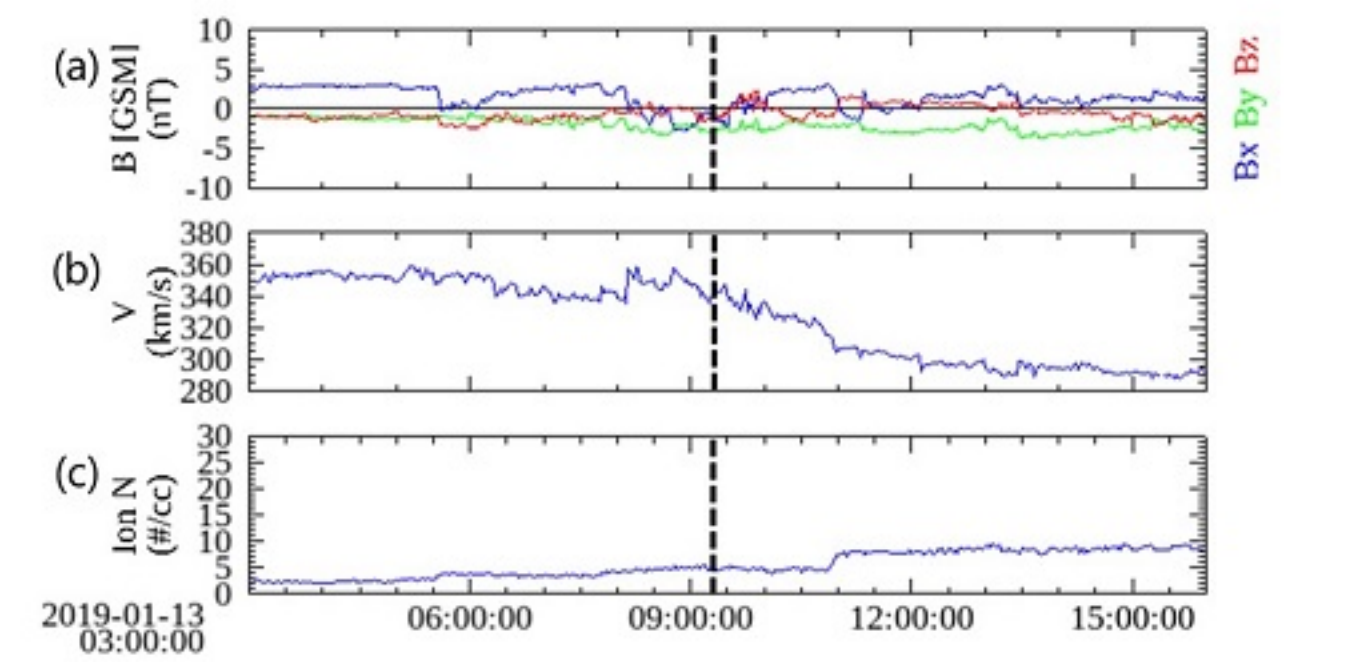
(a)
B [GSM] (nT)
10
5
0
-5
-10
Bx By Bz
(b)
V (km/s)
380
360
340
320
300
280
(c)
Ion N (#/cc)
30
25
20
15
10
5
0
2019-01-13
03:00:00
06:00:00
09:00:00
12:00:00
15:00:00

Figure 2.

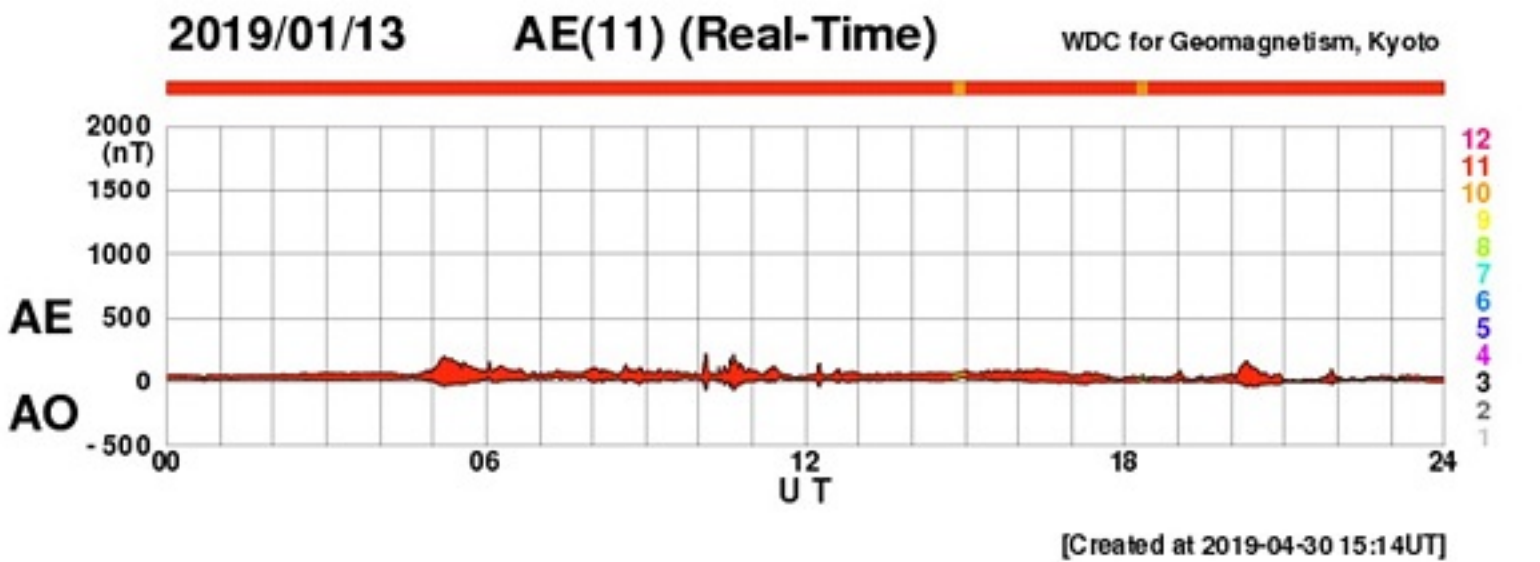
2019/01/13
AE(11) (Real-Time)
WDC for Geomagnetism, Kyoto
2000
(nT)
1500
1000
AE
500
0
AO
-500
00
06
12
18
24
U T
12
11
10
9
8
7
6
5
4
3
2
1
[Created at 2019-04-30 15:14UT]

Figure 3.

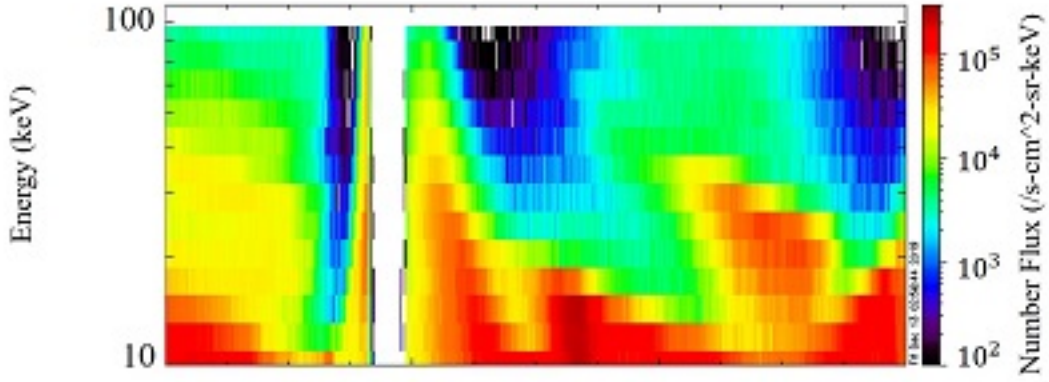

L	7.7	2.7	6.0	3.8
MLT	18.0	11.1	17.6	21.3
MLAT	29.1	-39.2	4.9	22.9
hhmm	00:00	04:00	08:00	12:00

Figure 4.

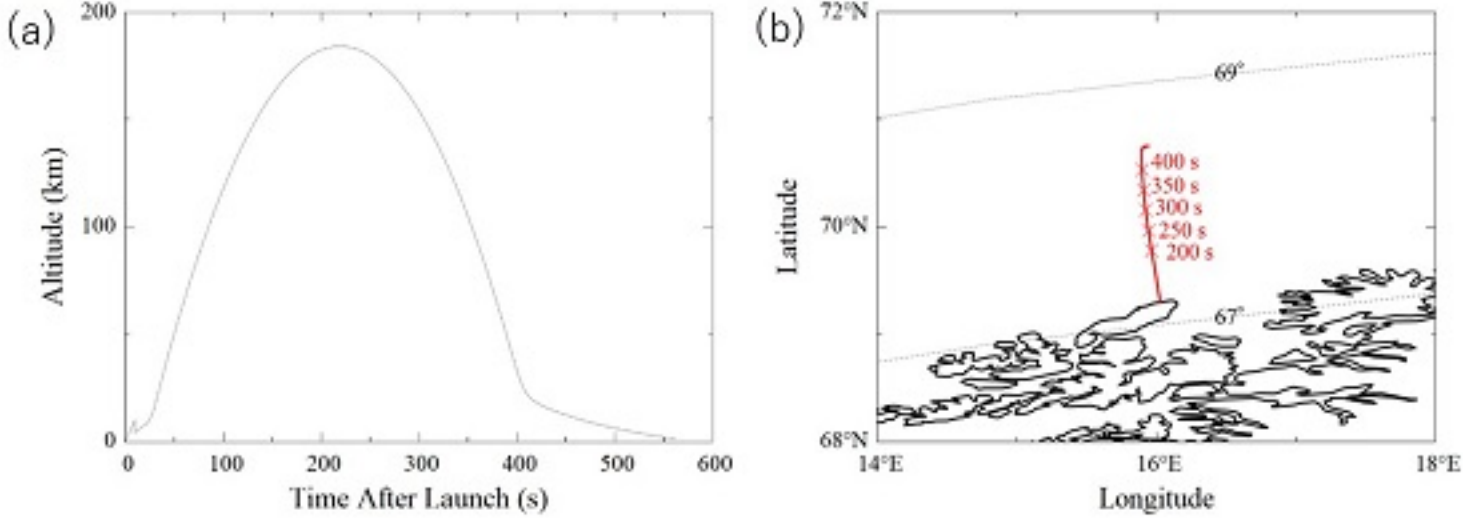
(a)
200
100
0
Altitude (km)
0
100
200
300
400
500
600
Time After Launch (s)
(b)
72°N
70°N
68°N
Latitude
69°
67°
400 s
350 s
300 s
250 s
200 s
14°E
16°E
18°E
Longitude

Figure 5.

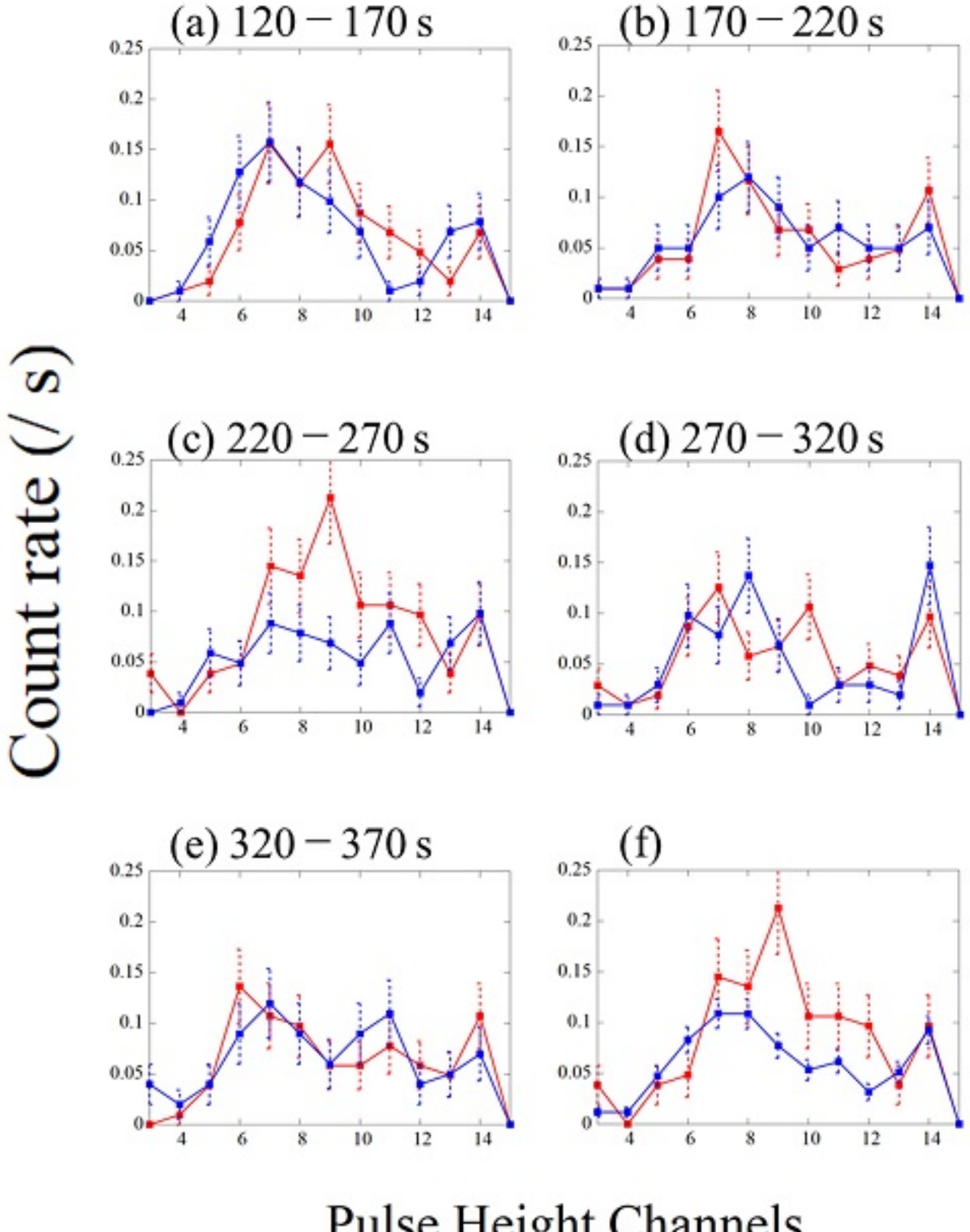
(a) 120 − 170 s
(b) 170 − 220 s
(c) 220 − 270 s
(d) 270 − 320 s
(e) 320 − 370 s
(f)
Count rate (/ s)
Pulse Height Channels

Figure 6.

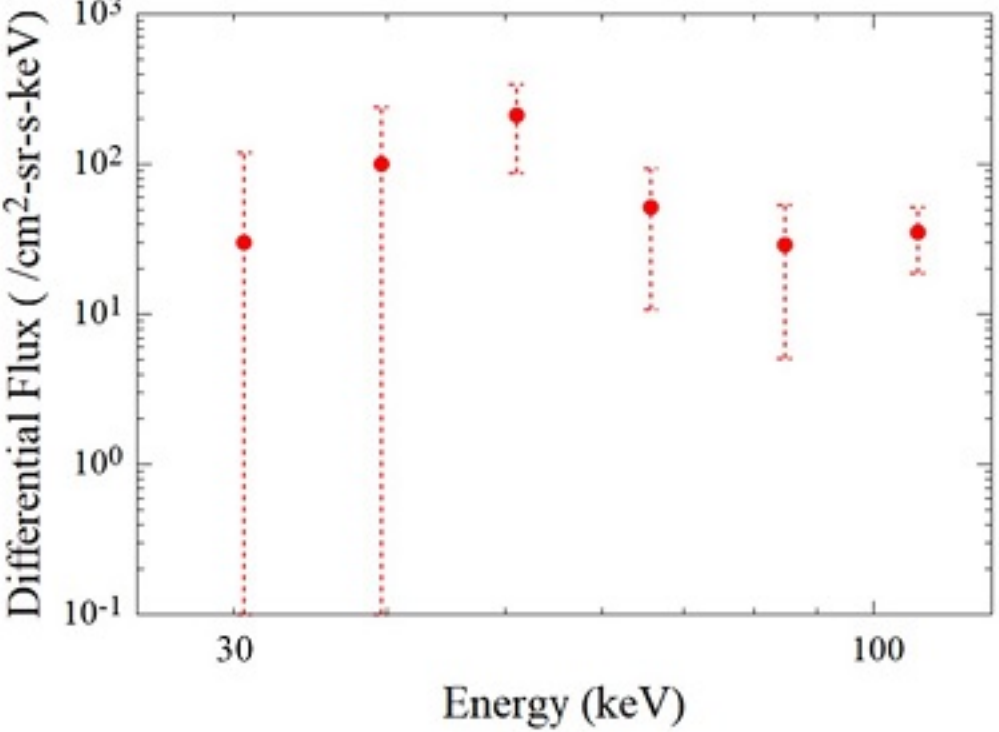
Differential Flux (/cm^2-sr-s-keV)
10^3
10^2
10^1
10^0
10^{-1}
30
100
Energy (keV)

Figure 7.

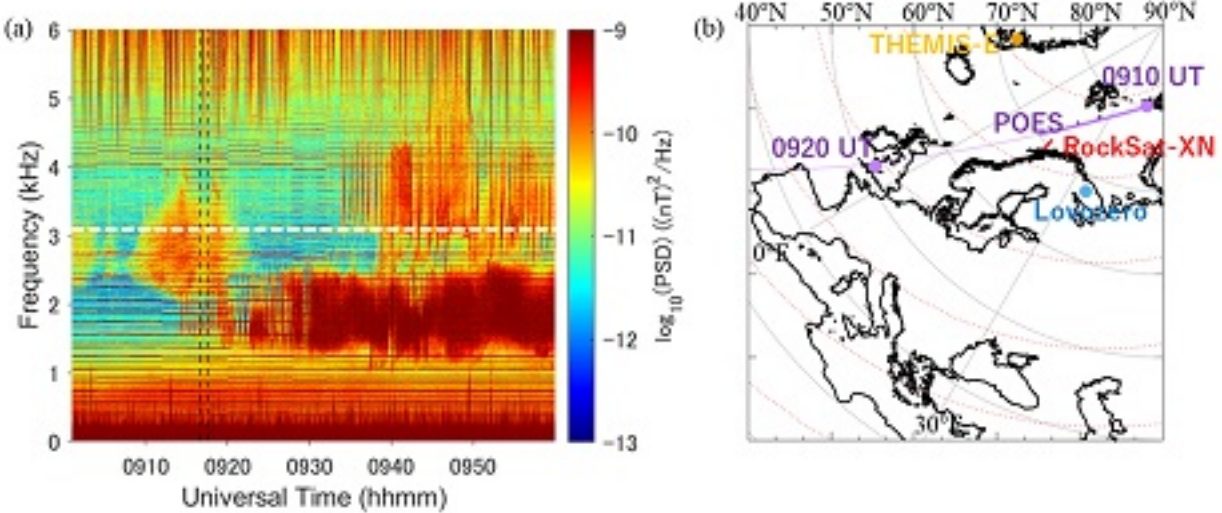
(a)
Frequency (kHz)
0
1
2
3
4
5
6
0910
0920
0930
0940
0950
Universal Time (hhmm)
−9
−10
−11
−12
−13
log10(PSD) ((nT)2/Hz)
(b)
40°N
50°N
60°N
70°N
80°N
90°N
THEMIS-E
0910 UT
POES
RockSat-XN
0920 UT
Lovozero
0°
30°

Figure 8.

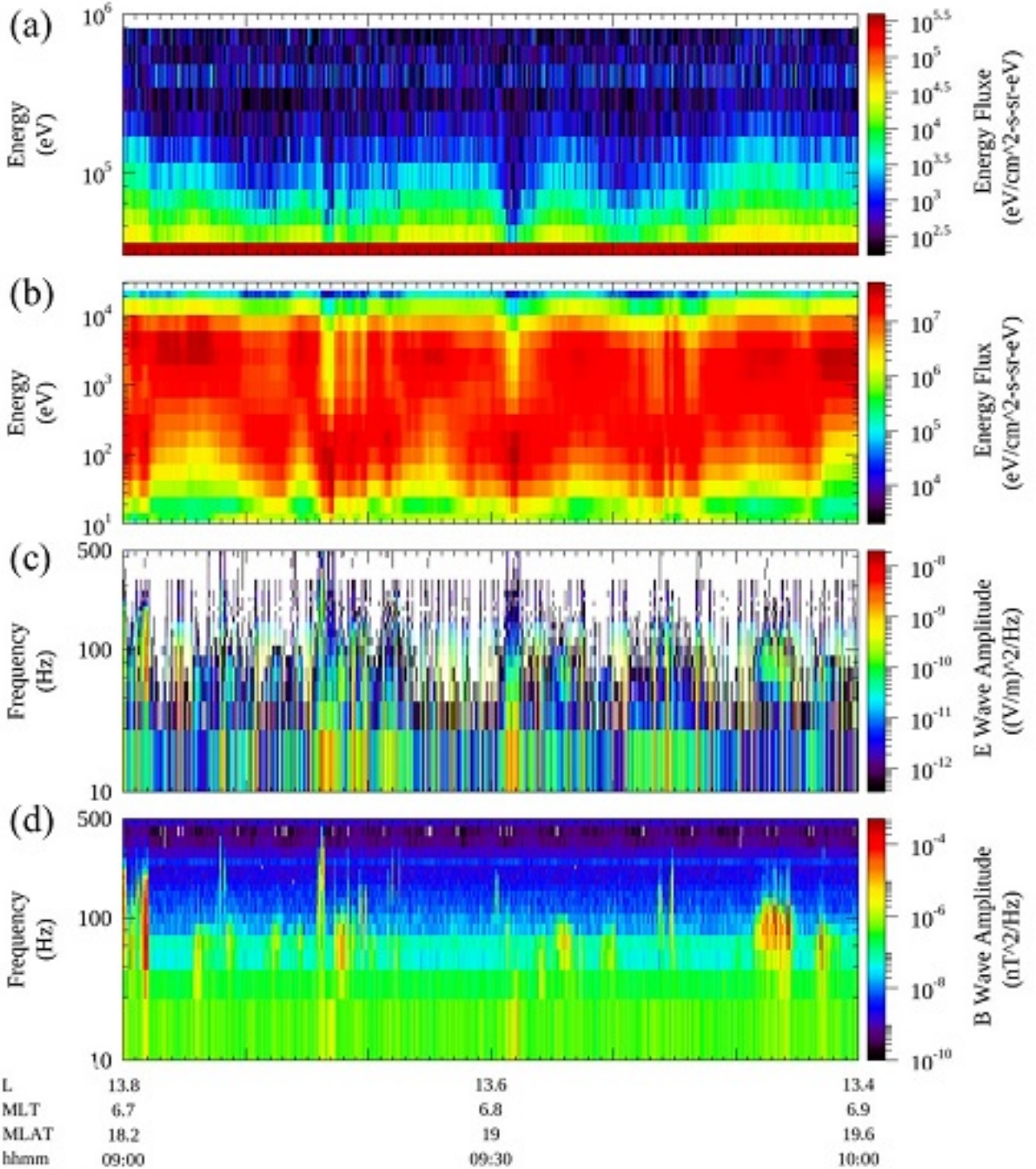
(a)
Energy (eV)
10^6
10^5
$10^{5.5}$
10^5
$10^{4.5}$
10^4
$10^{3.5}$
10^3
$10^{2.5}$
Energy Fluxe (eV/cm^2-s-sr-eV)
(b)
Energy (eV)
10^4
10^3
10^2
10^1
10^7
10^6
10^5
10^4
Energy Flux (eV/cm^2-s-sr-eV)
(c)
Frequency (Hz)
500
100
10
10^{-8}
10^{-9}
10^{-10}
10^{-11}
10^{-12}
E Wave Amplitude ((V/m)^2/Hz)
(d)
Frequency (Hz)
500
100
10
10^{-4}
10^{-6}
10^{-8}
10^{-10}
B Wave Amplitude (nT^2/Hz)
L 13.8 13.6 13.4
MLT 6.7 6.8 6.9
MLAT 18.2 19 19.6
hhmm 09:00 09:30 10:00
2019 Jan 13

Figure 9.

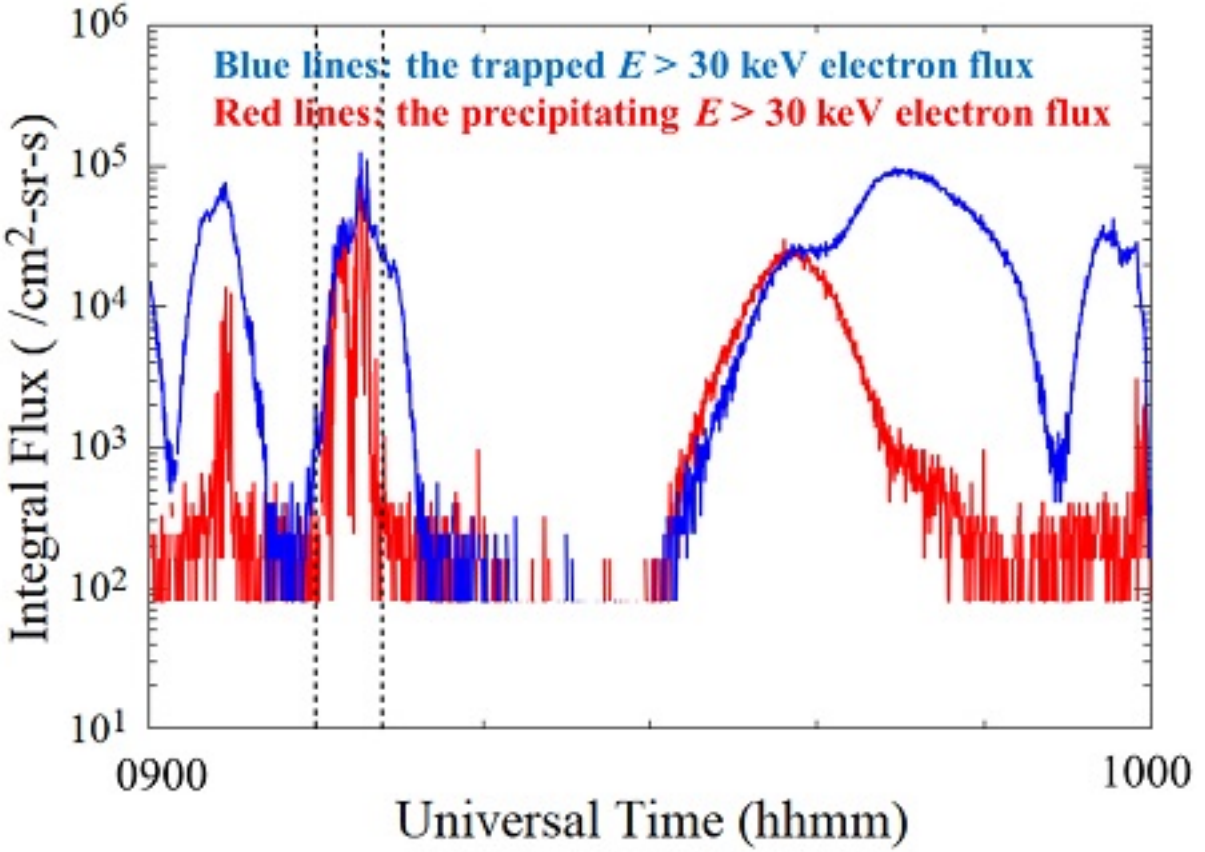
Blue lines: the trapped $E > 30$ keV electron flux
Red lines: the precipitating $E > 30$ keV electron flux
Integral Flux (/cm^2-sr-s)
10^6
10^5
10^4
10^3
10^2
10^1
0900
1000
Universal Time (hhmm)